PAPER

Check for updates

Stabilization of nanoporous Si/graphite composite anodes by ultrathin titanicone coatings

Tomas Kazda, [a] Raul Zazpe, [bc] Antonín Šimek, [b]
Jhonatan Rodriguez-Pereira, [bc] Ondřej Klvač, [ad] Juliana T. Hetzel, [e]
Ludek Hromadko, [c] David Pavlinak, [b] Sitaramanjaneya Mouli Thalluri, [b]
Mato Knez, [fg] Kurt W. Kolasinski *[e] and Jan M. Macak *[bc]

Herein, we report on the stabilization of nanostructured Si/graphite based anodes for Li-ion batteries (LIB) with titanicone against capacity fade and solid electrolyte interphase (SEI) formation. Nanostructured Si powders were first prepared by optimized and tailored Metal Assisted Catalytic Etching (MACE) of p-type Si wafers. These nanopowders were subsequently coated with titanicone thin films using molecular layer deposition (MLD) and extensively characterized in reference to uncoated nanopowders. The LIB anode slurry was prepared by blending 18 wt% uncoated or titanicone-coated Si nanopowder with graphite. The electrochemical performance of the anode containing coated Si was benchmarked against a corresponding electrode containing uncoated Si nanopowder. The titanicone-coated anode exhibited less reduction of the original capacity upon long-term cycling than the anode composed of graphite and uncoated Si nanopowder (51.1% versus 89.1%). The titanicone-coated Si anode also exhibited higher electrochemical activity during cyclic voltammetry measurements. The results demonstrate the power of ultrathin metalcone – in particular, titanicone – coatings for the improvement of the capacity and cyclability of Si/graphite based anodes.

Introduction

It is hard to imagine modern society without mobile, battery-powered portable devices, such as cell phones or notebooks. Together with the urgent need to reduce greenhouse emissions and the shift towards renewable energy sources, the impetus to develop highly efficient and long-term stable energy storage systems is growing. Lithium-ion batteries (LIBs) are currently the predominant battery system for energy-demanding applications. Their global production has been continuously increasing for years, and the forecast is that this trend will continue in the coming years.[1] However, the pursuit of new applications and improved performance place ever increasing demands on the

gravimetric energy density of LIBs as well as their lifespan, cost and sustainability.[2]

One of the most promising anode material technologies for future advancements in LIBs are Si anodes.[1–4] Silicon has numerous advantages, such as a high theoretical capacity of 3579 mAh g^{-1} (Li$_{15}$Si$_4$), approximately tenfold that of graphite (372 mAh g^{-1}), and a low potential of $\approx$0.4 V *vs.* Li/Li$^+$.[34] Another advantage is that silicon is the second most abundant element in the Earth's crust and its reserves are almost unlimited.[5] However, silicon also possesses several disadvantages, such as its large volume change ($\sim$300%) during lithiation/delithiation (which leads to particle cracking, degradation of contact with other parts of the electrode and the current collector), high irreversible capacity and continuous growth of the solid electrolyte interphase (SEI) layer.[6] All this leads to a rapid capacity drop during cycling, subsequent low Coulombic efficiency and reduced cycle life. Overall, these are the main reasons why anodes exclusively comprising Si are rarely used in LIBs.

However, there are some ways to enhance the performance of a Si anode. The first one is to create Si/C composite anodes that use materials such as amorphous carbon, graphite, carbon nanotubes (CNTs), carbon nanofibers (CNFs), graphene, or metalorganic frameworks (MOFs).

The second approach, which is particularly effective for mitigation of deleterious effects of expansion and contraction,

a Department of Electrical and Electronic Technology, Faculty of Electrical Engineering and Communication, Brno University of Technology, Brno, Czech Republic

b Central European Institute of Technology, Brno University of Technology, Brno, Czech Republic

c Center of Materials and Nanotechnologies, University of Pardubice, Pardubice, Czech Republic. E-mail: jan.macak@upce.cz

d Thermo Fisher Scientific Brno, Vlastimila Pecha 12, Brno, 627 00, Czech Republic

e Department of Chemistry, West Chester University, West Chester, PA 19380, USA. E-mail: kkolasinski@wcupa.edu

f CIC NanoGUNE, Tolosa Hiribidea 76, E-20018 San Sebastian, Spain

g Ikerbasque, Basque Foundation for Science, Plaza Euskadi 5, Bilbao E-48009, Spain

relies on nanostructuring of Si, leading to considerably improved reversibility during lithiation/delithiation cycles.[7–12] Thin films, pillars/nanowires,[13–15] and porous Si[9] were all shown to improve the reversibility as compared to bulk silicon. Crystalline Si nanowires (SiNW) with a cross section below 150 nm[16] and amorphous pillars with a cross section below 870 nm[17] retain their structural integrity upon cycling. Porosification was shown to improve the cycling behavior.[17]

However, for the practical implementation of LIB at scale, the nanostructuring of powders rather than wafers is required.[18] The earliest attempts to porosify Si powders used stain etching.[19–22] Such powder, unfortunately, has much too high surface area that accompanies its narrow ~ 4 nm pores. High surface area promotes heavy SEI formation. Larger pores and lower surface area can be obtained with metal assisted catalytic etching (MACE). Fortunately, Si crystallizes relatively easily during conventional powder particle formation and polycrystalline grains exhibit crystallographically dependent etching during MACE much like that of single-crystal wafers.[23] Several groups were able to implement MACE with Si powders[24–29] and several used this material in LIB anodes.[30–32] Overall, the utilization of Si in commercial batteries was successfully initiated,[33] but improvements in performance are still urgently sought after.

A promising method to improve the properties of Si anodes is the formation of a surface coating that acts as a buffer for the volume change and, simultaneously, as an interface between the Si surface and the electrolyte.[6,34] Pioneering papers on the use of ultrathin protective coatings of anodes prepared by atomic layer deposition (ALD) against the formation of a SEI have recently appeared. They include mainly alumina, titania and zinc oxide coatings.[35–40] However, these coatings are brittle and not suitable for protecting Si, regardless of its shape and morphology, due to its larger volume expansion, especially during lithiation.

There is a class of vapor phase grown materials named "metalcones", which are inorganic–organic hybrid materials grown by introducing organic monomers into an ALD process. This process is called molecular layer deposition (MLD). Based on the metals contained, the materials are called alucone, zincone, niobicone or titanicone, if they contain Al, Zn, Nb or Ti, respectively.[41–45] Among the key advantages of metalcones, as opposed to inorganic materials, is their considerably higher flexibility and adaptability to volume changes in advanced anode materials, as described in a review article by Zhu et al.[46] Mu et al.[47] demonstrated the use of zincone coatings in combination with pure Si. The resulting electrode exhibited higher capacitance and stability compared to the Si electrode fabricated using silicon nanoparticles. Fang et al.[41] coated Si nanowires with niobicone, which were then annealed at 500 °C. The coating increased the electrode's capacitance, cyclability and stability at a higher C-rate. Luo et al.[48] focused on the comparison of ALD Al_2O_3 coatings with MLD alucone coatings. It was found that the alucone coating increased the lithiation level of Si nanowires compared to an Al_2O_3 coating. Huertas et al.[49] demonstrated the use of titanicone coating on commercial Si nanoparticles (Alfa Aesar) and subsequent drying at 150 °C. The particles coated with titanicone exhibited higher stability and capacity than the Si particles without treatment.

However, until now, there is no report that demonstrates sufficient protection of Si nanopowders, produced by MACE, from SEI formation with comprehensive performance figures. Therefore, by utilizing state-of-the-art knowledge and equipment, we introduce in this paper titanicone coating of Si nanopowders by MLD and create a graphite/Si anode composed of the thus obtained Si-titanicone nanopowders. In comparison to benchmark anodes, composed of uncoated Si nanopowders, the coated-nanopowder anodes exhibit superior capacity and cyclability, as demonstrated by electrochemical characterizations.

Materials and methods

Nanostructured silicon particles synthesis

Silicon powders were obtained by grinding of highly doped p-type wafers (0.01–0.02 Ω cm, University Wafer), sufficient to pass through a 44 μm mesh. After grinding the powders were sonicated for 1 h in 3% H_2O_2 (Acros Organics 35% ACS reagent) to remove organic and metal contamination, rinsed with deionized water, filtered coarsely to remove <2 μm particles (Whatman grade 42 filter paper), and dried in a vacuum oven. All reagents were Fisher ACS reagents, unless otherwise specified.

To optimize cycling behavior, high pore volume, low surface area porous silicon with sufficiently large pores (10–20 nm) to facilitate facile lattice expansion during lithium transport is required. By using a low load of metal catalyst during MACE, mesoporous with these characteristics rather than macroporous silicon is formed.[50] We optimized etching with a Cu catalyst, based on the process previously reported by Kolasinski and co-workers.[51] The choice of highly doped p-type material and a Cu catalyst were made because they represent the best option for high-yield production of large-pore, low-surface-area material made with an inexpensive metal catalyst. Other combinations of doping levels, etching temperature and metal catalyst are possible options. Si powder was dispersed in glacial acetic acid and cooled in an ice water bath. Under constant stirring, concentrated HF (Acros Organics 49% ACS reagent) was added slowly to produce a solution that is ultimately 2 parts HF to 1 part acetic acid by volume, and chilled for 10 min before adding Cu^{2+} in the form of a 6 mM aqueous $CuSO_4$ solution. $CuSO_4$(aq) was added over a 15 min period via an injection pump (kd Scientific Legato 100) such that 25 μmol per gram of Si was deposited. After injection, the ice was removed, and the water bath and solution were brought to 20 °C. A sufficient amount of H_2O_2 was injected over a 75 min period to deliver a quantity measured in moles of H_2O_2 that is equal to Si. The etched powder was rinsed with 0.2 M HCl(aq), deionized water, ethanol and finally wetted with pentane before drying in a vacuum oven at 50 °C overnight. To convert the initially hydrogen-terminated and hydrophobic silicon into a hydrophilic material suitable for MLD, partial oxidation of the Si surface was performed at 300 °C in air for 4 h in a box furnace.

MLD coating

Fluidized bed molecular layer deposition (FB-MLD) was used for the coating of Si particles with titanicone at a deposition

temperature of 120 °C using an ALD reactor (TFS 200, Beneq). The precursors were titanium tetrachloride (TiCl$_4$, electronic grade 99.9998%, STREM) and ethylene glycol (EG, anhydrous 99.8%, Sigma-Aldrich). EG was heated to 80 °C to obtain sufficiently high vapor pressure. To maximize the number of active surface sites (mainly hydroxyl groups), the Si particles were pre-treated with 10 pulses of water vapor of 10 s duration, followed by a purge time of 60 s. Subsequently, the Si particles were coated with 50 MLD cycles of titanicone. One MLD cycle was defined by the following sequence: TiCl$_4$ precursor (9 s)-N$_2$ purge (60 s)-EG precursor (45 s)-N$_2$ purge (300 s). N$_2$ (99.9999%) was used as the carrier gas at a flow rate of 100 standard cubic centimeters per minute (sccm). To avoid particle agglomeration and facilitate Si particle dispersion, the reactor was agitated with mechanical vibration.

Electrode preparation and electrochemical testing

Si particles and Si-titanicone particles were mixed with graphite (20 : 80 weight ratio) in a ball mill (Fritsch) at 300 RPM for 30 min in a mixture of H$_2$O with Ethanol (50 : 50). The ratio of sample and balls was 1 : 10. The resulting Si/Gr composite and Si-Tit/Gr composite were mixed with carbon Super P and CMC (carboxymethyl cellulose) binder in a 90 : 5 : 5 weight ratio. A mixture of water and ethanol (50 : 50 vol%) was used as solvent. After 24 hours of mixing, the resulting slurry was applied to the Cu foil using a 200 μm coating bar. The deposited layer was then dried at 60 °C. Subsequently, disc electrodes with a diameter of 18 mm (2.54 cm^2) were cut and pressed with a pressure of 500 kg cm^{-2}. The electrodes were dried under vacuum at 110 °C for 24 hours and subsequently transferred to a glove box (Jacomex) with Ar atmosphere. The electrodes were inserted into electrochemical test half cells ECC-STD (El-Cell@) and a lithium metal disc was used as counter electrode. Fiberglass was used as a separator which was filled with electrolyte 1 M LiPF$_6$ dissolved in ethylene carbonate (EC) and dimethyl carbonate (DMC) in the ratio EC : DMC 1 : 1 (v:v) (Sigma Aldrich).

The cells were cycled using a 16-channel Biologic VMP3 potentiostat between 0.01 V and 2.5 V vs. Li/Li$^+$ at various C-rate from 0.1C to 1C and at 0.2C for 100 cycles at room temperature. The obtained capacities were related to the weight of active mass of Si/Gr or Si-Tit/Gr composite. The active mass loading averaged about 3.8 mg cm^{-2}. The calculated capacity of the Si/Gr (3579 mAh g^{-1}/372 mAh g^{-1}) mixture for 1C was 1013 mAh g^{-1}. Cyclic voltammetry (CV) was carried out using Biologic VMP3 in the potential range of 0.01–2.5 V vs. Li/Li$^+$, at 0.1 mV s^{-1} scan rate for 4 cycles. Electrochemical impedance spectra (EIS) were measured within the frequency range from 0.01 Hz to 1 MHz with an alternating current voltage amplitude of 10 mV.

Characterization

The morphological features of the Si nanopowders before and after MLD coatings were characterized using a field-emission scanning electron microscope (FE-SEM, JEOL, JSM 7500 F). Proprietary Nanomeasure software was used to measure the average pore size (diameter value) after the MLD process.

The surface chemical composition of Si nanopowders coated with titanicone by MLD and the post-performance battery anode was assessed by X-ray photoelectron spectroscopy (XPS). The measurements were performed using an ESCA2SR system (Scienta-Omicron) with a monochromatic Al Kα (1486.7 eV) X-ray source operated at 200 W. The compensation of the surface charge of the samples was controlled with an electron gun (CN 10) operated at 5 μA and 1.0 eV. The binding energy scale was referenced using adventitious carbon (284.8 eV). Quantitative analysis was performed with CasaXPS software (Casa software Ltd) using the elemental sensitivity factors provided by the manufacturer.

The battery electrodes were analyzed using the cross-sectional analyses, with sample preparation performed with a Thermo Scientific CleanMill Broad Ion Beam (BIB). The instrumentation setup utilizes an adaptation to the Thermo Scientific CleanConnect Sample Transfer System, which enables the transfer of air-sensitive samples between the glovebox, BIB, and SEM maintaining an argon atmosphere, and preventing sample contamination while preserving sample integrity. SEM imaging and EDS analysis were conducted using a Thermo Scientific Scios 2 instrument with an UltraDry EDS detector.

X-ray diffraction (XRD) patterns of Si nanopowders with and without titanicone as well as postmortem samples were measured with a Panalytical Empyrean diffractometer at grazing incident geometry. The incidence (omega) angle was set to 2°. The sample was measured through a range of 10–80° (2 Theta). A Cu Kα tube was used as the X-ray source.

Nitrogen adsorption porosimetry with combined Brunauer–Emmett–Teller (BET) and Barrett–Joyner–Helenda (BJH) analysis was performed with a Micromeritics ASAP2020 Plus porosimeter.

Results and discussion

Fig. 1 shows SEM images of the Si nanopowders before (as produced by MACE) and after titanicone MLD. One can see the presence of roughly 20 nm nanopores, uniformly distributed over the exterior of the particles. After MLD, the surfaces become less conducting, due to the hybrid titanicone coating on the surface, and thus more challenging for SEM inspection. Nonetheless, one can see that the nanoporous characteristics of the sample were preserved. In terms of textural properties, as determined by nitrogen absorption porosimetry, the Si nanopowders are characterized by typical BET specific surface areas of 50–55 m^2 g^{-1}, BJH pore volume of 0.27 ± 0.02 cm^{-3} g^{-1} and mean pore size of 16.5 ± 1 nm. The estimated porosity is approximately 39%. The distribution of pores is shown in Fig. S1. The results of this measurement fit to the pore sizes observed by SEM in Fig. 1. According to the available literature, the nominal growth rate of titanicone using these precursors and at the deposition temperature of 120 °C is around 0.45 nm per cycle.[42] This means that after 50 cycles we would deposit around 22.5 nm of titanicone coating on Si powders. However, the average pore size (diameter value) after the MLD process estimated from SEM images was reduced from 16.5 ± 1 nm to 7.8 ± 1.39 nm, which means that a titanicone coating thickness
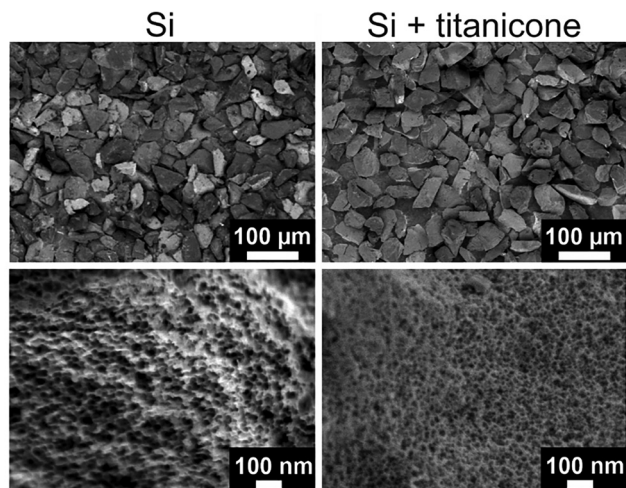
Fig. 1 SEM top-view images of a Si particle taken at two different magnifications. Left column: After porosification with MACE using Cu nanoparticles. Right column: After MLD of titanicone.

Fig. 2 XPS spectra of Si particles after MLD deposition of titanicone: (a) survey, (b) C 1s, (c) O 1s and (d) Ti 2p.

of around 4.35 nm (0.087 nm per cycle) was achieved. The lower growth rate found experimentally by us, as compared to the value reported in the literature, is ascribed to the different nature of the substrates. The value cited in ref. 42 deals with native oxide (SiO_2) on Si wafers. In our case, the surface of the Si powder likely offers a lower number of active sites on the surface to promote the growth of titanicone, leading to a lower growth rate.

Fig. S2 shows XRD patterns of the samples shown in Fig. 1. Only Si patterns are visible. There is no titanicone peak visible, which is likely either due to the amorphous nature of the layers, or because the concentration is below the detection limit of X-ray diffraction. Therefore, a more surface-sensitive technique was needed to analyze the presence of titanicone on the surface of Si.

XPS analysis was carried out to characterize the surface chemical composition of Si-titanicone particles. The presence of C, O, Ti, Cl and Si was detected as shown in Fig. 2a and the quantification in Table S1. C may be related to both adventitious carbon and the MLD titanicone, as well as O and Ti. Cl is a remnant from the Ti precursor used for the MLD process. Si corresponds to the Si particles. The C 1s high resolution spectrum (Fig. 2b) shows four chemical species. At 284.8 eV the component corresponds to adventitious carbon or C–(C,H). At 286.0 eV the signal with higher intensity is related to C–OH. At 287.3 eV the component is associated to C=O and at 289.0 eV the species is COOH.[52,53] The O 1s spectrum (Fig. 2c) also exhibited four different chemical environments. At the lower binding energy, 530.2 eV, the peak is assigned to oxygen bound to Titanium (Ti–O).[54] The peak denoted by the blue line is related to –OH groups or C=O at 531.4 eV.[55] The peak denoted by the green line at 532.6 eV corresponds to C–OH and the peak denoted by the orange line at 533.8 eV is assigned to COOH.[56] The Ti 2p spectrum (Fig. 2d) showed the corresponding spin–orbit splitting Ti $2p_{3/2}$/Ti $2p_{1/2}$. The spectrum was fitted with two contributions that correspond to one chemical state. The signals
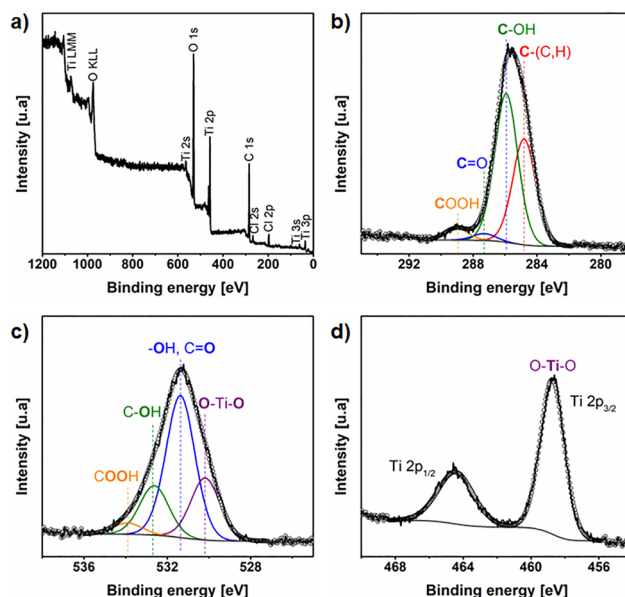
centered at ∼458.7/464.4 eV were assigned to Ti^{4+} (O–Ti–O).[55,57] These results confirm the successful titanicone MLD deposition on Si particles.

During the first step of electrochemical tests, the first set of electrodes were tested in electrochemical cells (ElCell) by CV and then by cycling under various C-rates. Fig. 3a shows CV profiles of the Si/Gr and Si-Tit/Gr anodes at a scan rate of 0.1 mV s^{-1}. The profiles of both electrodes are similar, but the Si-Tit/Gr anode achieves higher currents. Anodic and cathodic peaks of Si-Tit/Gr and Si/Gr anodes occur at similar positions. From the CVs one can distinguish peaks related to the graphite and the Si electrochemical activity. The anodic peaks at 0.28 V and 0.5 V and the cathodic peaks at 0.15 V and 0.065 V are related to Si. Similar peaks were described by Jerliu et al.[58] Especially the silicon cathodic peak at 0.15 V is significantly more evident and sharper in the Si-Tit/Gr anode.

This may indicate higher Si activity and better reaction kinetics. These improvements are consistent with the findings of Huertas et al.,[49] where they reported that MLD coating improves lithium-ion transport and electronic conductivity across the electrode surface and helps form a more stable SEI. Fig. 3b shows the cycling of the Si/Gr and Si-Tit/Gr anode at different C-rates from 0.1C to 1C. The Si-Tit/Gr anode achieved a higher capacity than the Si/Gr anode at 0.1C, 0.2C and 0.5C. Capacity in the first cycle at 0.1C for Si-Tit/Gr anode was 603 mAh g^{-1} and efficiency 96.4%. For Si/Gr anode, it was 526 mAh g^{-1} and 93.7% efficiency. In the second cycle was capacity 583 mAh g^{-1} and efficiency 97.0% for Si-Tit/Gr anode and 510 mAh g^{-1} and efficiency 93.8% for Si/Gr anode. At the highest C-rate, 1C, the capacities were about 60 mAh g^{-1} for both anodes.

The second set of electrodes was tested using a current of 0.2C for 100 cycles. In the first step, the electrodes were cycled with a current of 0.1C for three cycles, see Fig. 4a. The charging
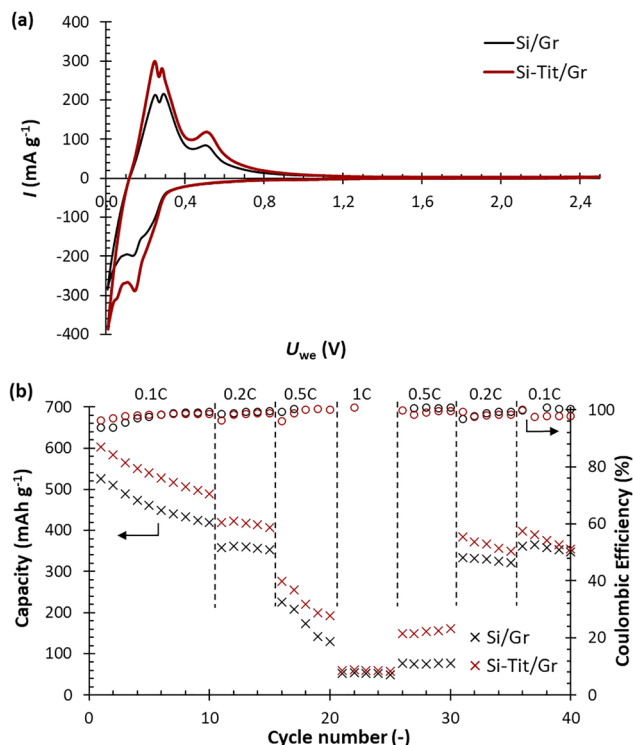
Fig. 3 (a) Cyclic voltammetry of Si/Gr and Si–Tit/Gr anode at 0.1 mV s^{-1}, fourth cycle. (b) Comparison of the cycling at different C-rates from 0.1C to 1C of Si/Gr and Si–Tit anodes.

capacity in the first cycle of the Si/Gr anode was 1065 mAh g^{-1} and the discharging capacity was 900 mAh g^{-1}. The irreversible capacity in the first cycle was therefore 15.5%. The discharging capacity in the second cycle was 790 mAh g^{-1} and the irreversible capacity was 10.9%. In the case of the Si–Tit/Gr anode, the charging capacity in the first cycle was 807 mAh g^{-1} and the discharging capacity was 696 mAh g^{-1}. The irreversible capacity was therefore 13.8%. In the second cycle, a discharging capacity of 663 mAh g^{-1} was achieved and the irreversible capacity was 5.5%. In the third cycle, the capacity Si/Gr anode (687 mAh g^{-1}) dropped to the level of the capacity of the Si–Tit/Gr anode (640 mAh g^{-1}). Fig. 4b shows the differential capacity analysis during delithiation in the first three cycles for the Si/Gr anode. The graph shows that the size of the peaks at potentials of 0.11 V and 0.15 V gradually decreased; a similar decrease was also evident in the peak at a potential of 0.45 V. We also observed a gradual narrowing of this peak. Differential capacity analysis during delithiation in the first three cycles for the Si–Tit/Gr anode is shown in Fig. 4c. Peaks in similar areas are observed, as in Fig. 4b, with the size of the peaks being very similar during the three cycles and, at the same time, the width of the peak at a potential of 0.45 V being the same in the second and third cycle. Heubner et al.[59] and Loveridge et al.[60] describe that this peak is purely related to the delithiation of Si from Li$_2$Si to Si. The lower peaks at potentials of 0.11 V and 0.15 V represent the activity of graphite. It can be concluded that the stable activity of the Si–Tit/Gr anode at a potential of 0.5 V is due to the stabilizing effect of the titanicone MLD coating.
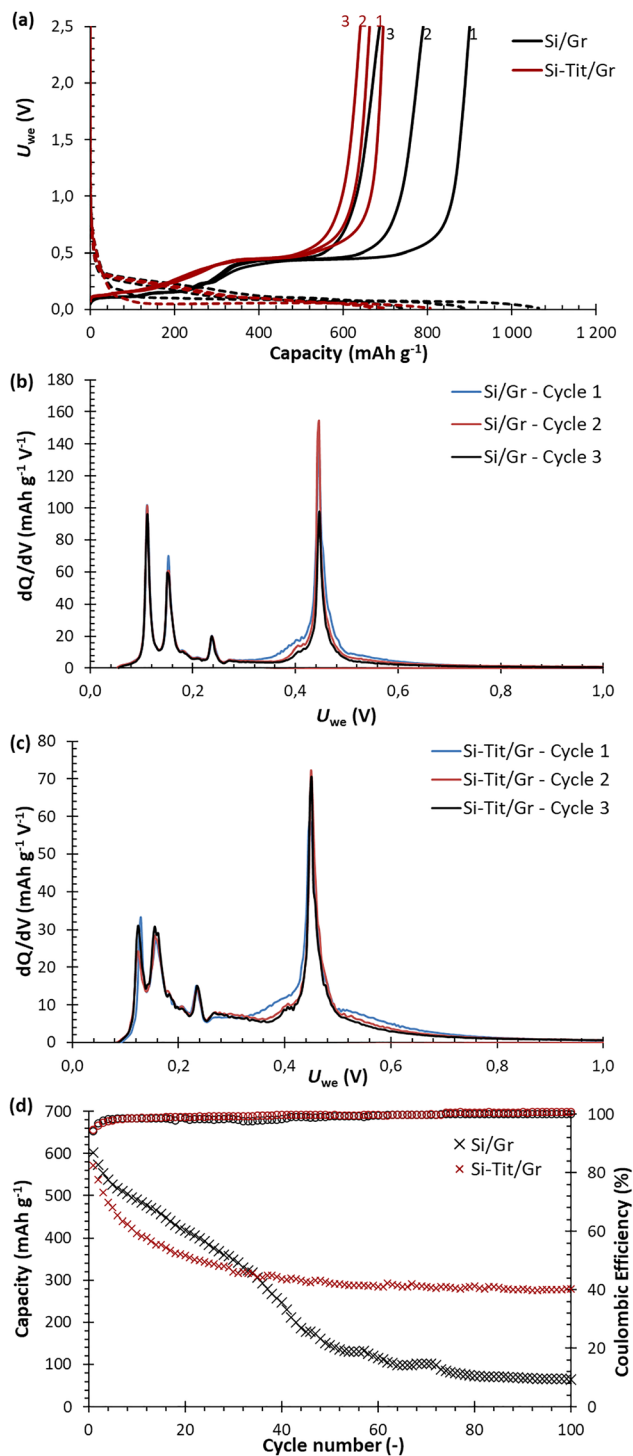

Fig. 4 (a) Comparison of the first 3 cycles of Si/Gr and Si–Tit/Gr anodes at 0.1C before 100 cycles at 0.2C, differential capacity analyses during delithiation in the first three cycles for the Si/Gr anode (b) and the Si–Tit/Gr anode (c), respectively, (d) Galvanostatic cycling of Si/Gr and Si–Tit/Gr anode at 0.2C Ti 2p.

The electrode with pure Si then loses Si activity much faster. These data correlate well with the CV result, where the peak related to Si activity was more noticeable. After the first 3 cycles at a current of 0.1C, followed cycling at 0.2C for 100 cycles, see

Fig. 4d. The Si/Gr anode reached a capacity of 602 mAh g^{-1} and the Si-Tit/Gr electrode reached a capacity of 571 mAh g^{-1} at the beginning of cycling. The efficiency in the first cycle was 94.2% for the Si/Gr anode and 95.2% for the Si-Tit/Gr anode in the first cycle. However, the capacity of the Si/Gr anode decreased more rapidly and after 100 cycles capacity decreased to 65 mAh g^{-1}, which corresponds to a 10.9% capacity retention. In the case of the Si-Tit/Gr anode, the capacity decrease decelerated during cycling and was relatively stable in the second half of cycling. In the last cycle a capacity of 280 mAh g^{-1} was attained, which corresponds to a 49% capacity retention. Overall, the positive effect of the titanicone coatings on the anode performance was clearly demonstrated with these results. Titanicone coating led to improved Si stability and formation of a more stable SEI, which resulted in the lower irreversible capacity described above and more stable Si activity in differential capacity analysis.

In terms of the literature available, Fang et al.[61] presented Si nanofibers stabilized by niobicone coating by MLD. With a significantly lower loading of 0.76 mg cm^{-2} and with 60% active material in the electrode, a capacity retention of 38% was observed for their electrode after 120 cycles. Pillai et al.[62] presented the use of a Si-graphite composite, where Si was pre-treated by MACE. The Si content in the electrode was 20% and the loading was again significantly lower (1.62–2.66 mg cm^{-2}) than in this work (3.2 mg cm^{-2}). After 100 cycles at 0.1C they observed a capacity retention of 38%, while in the present work it was 49%. Son et al.[63] investigated the rapid degradation of a graphite-Si composite anode with a Si content of 15%, and obtained an initial capacity of 918 mAh g^{-1} when cycling at a current of 0.1C, with a capacity retention of 36%.

A comparison of our material's performance against performances shown in existing publications (which have observed lower or similar capacity retention, however with significantly lower active mass loading) is shown in Table 1. It is noteworthy that in all these works, authors used 10–20% of binder in the electrode, whereas in our case the binder content was only 5%, which is beneficial as there is more active material in the anode rather than electrochemically passive binder.

At the end of cycling at 0.2C, the Si-Tit/Gr anode was removed from the electrochemical cell (ElCell) in a glove box. Subsequently, part of the electrode was transferred to the SEM for postmortem cross-sectional analysis. The results are shown

in Fig. 5a. The figure shows the surface part of the Si-Tit/Gr electrode in a cross-sectional view. One can see that the electrode is porous and is composed of interconnected individual graphite particles.

The center of the image shows a material with a different density, which is reflected by the contrast change. Several points in the figure, marked with a number, were selected for EDS analysis, and the results of the analyses are shown in Table 2. According to the EDS map in Fig. 5b–e, one sees a fairly uniform distribution of carbon, i.e. graphite, in the center, then Si particles, which are shown on the EDS map in Fig. 5c. The Si particles are surrounded by graphite or integrated into it. At the same time, one observes that on all particles there are residues of phosphorus, which is a component of the electrolyte and is part of the SEI layer on the surface of the particles after cycling, see Fig. 5d. In the places where Si is present, the presence of Ti is visible. It is therefore evident that even after cycling, Ti species are still present on the Si particles, see Fig. 5e.

Similar analysis was performed after cycling of the Si/Gr electrode, as shown in Fig. 6. The Si/Gr electrode in the cross-sectional view is shown in Fig. 6a. One can see a porous electrode, whose upper region is less porous. Several points in the figure, marked with a number, were selected for EDS analysis, and the results of the analyses are shown in Table 3.

Fig. 6b exhibits the carbon distribution, where it is shown that graphite migrated to the top and the bottom of the electrode. Fig. 6c demonstrates that the center of the electrode is composed of Si particles, which are very porous due to the volume change during the cycling. Cycling leads to a significant increase in porosity and, therefore, of the total electrode thickness. A greater separation of carbon from Si is also seen in Table 3 for points 3 and 5. Fig. 6d shows the distribution of phosphorus (P) within the electrode. The P concentration is slightly lower on spots where the Si particles are located. Fig. 6e shows the distribution of oxygen within the electrode, which is most strongly correlated with the presence of Si particles. Comparing the cycled Si-Tit/Gr and Si/Gr electrode, the Si particles are surrounded by graphite particles and are in relatively good contact for the Si-Tit/Gr electrode. However, in the case of the Si/Gr electrode, the structure is rather disturbed and individual Si particles are detached from graphite particles, which are significantly damaged. These results correlate with the findings of Son et al.,[63] who observed a similar phenomenon in MLD-coated Si-graphite electrodes, where uncoated electrodes

Table 1 Comparison of LIBs performance of the present work with previously reported results

Type of electrode	Si%/active material loading	C-Rate	Number of cycles	Initial capacity [mAh g^{-1}]	Capacity retention [%]	Ref.
MACE based Si/graphite composite	20%/1.62–2.66 mg cm^{-2}	0.1C	100	786	38	62
Si Nanoparticles coated with titanicone	60%/0.84 mg cm^{-2}	1C	350	1180	94	49
Si-nonographite aerogel-based (SNGA/NG)	20.8%/1 mg cm^{-2}	0.09C	30	1050	58	64
MACE based porous Si nanowires	70%/1 mg cm^{-2}	0.2 A g^{-1}	100	3530	7	65
Si zincone MLD coating (Si@50-ZC)	80%/1.05 mg cm^{-2}	0.2 A g^{-1}	100	3093	26	47
Si NW@NbHQ-500	60%/0.76 mg cm^{-2}	0.2 A g^{-1}	120	3200	38	61
Si@Graphene composite	60%/0.5 mg cm^{-2}	0.2 A g^{-1}	100	3578	53	66
G–Si composite	15%/	0.1C	100	918	36	63
Si-Tit/Gr	18%/3.2 mg cm^{-2}	0.2C	100	571	49	This work

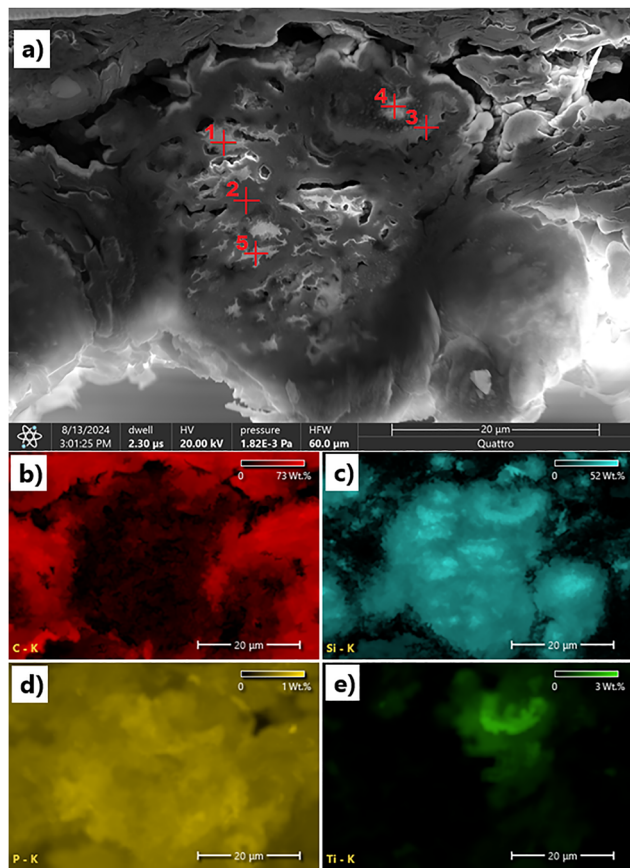**Fig. 5** (a) SEM cross-sectional image of Si-Tit/Gr anode after cycling (horizontal field width ≈60 μm). EDS maps of the distributions of (b) carbon, (c) silicon, (d) phosphorus, and (e) titanium.

Fig. 6 (a) SEM cross-sectional image of Si/Gr anode after cycling (horizontal field width ≈60 μm). EDS maps of the distributions of (b) carbon, (c) silicon, (d) phosphorus, and (e) oxygen.

Table 2 Results of EDS analysis of Si-Tit/Gr anode cross section after cycling, points 1 to 5 (as shown in Fig. 4a)

Anode	Weight (%)				
Element	Point 1	Point 2	Point 3	Point 4	Point 5
C	8.2	9.5	13.1	20.7	9.2
O	55.4	44.2	61.1	41.2	62.6
F	4.8	1.2	3.7	3.1	4.6
Si	31.1	41.4	20.8	9.8	23.4
P	0.3	2.0	0.3	0.4	0.2
Cu	0.2	1.7	0.2	24.3	0.0
Ti	0.0	0.0	0.8	0.3	0.0

Table 3 Results of EDS analysis of Si/Gr anode cross section after cycling, points 1 to 5 (as shown in Fig. 5a)

Anode	Weight (%)				
Element	Point 1	Point 2	Point 3	Point 4	Point 5
C	42.8	18.9	52.2	7.2	56.9
O	21.3	51.9	38.9	60.1	19.6
F	1.8	6.9	4.3	4.2	3.0
Si	33.2	21.3	2.4	27.4	1.5
P	0.3	0.4	0.6	0.4	0.9
Cu	0.6	0.6	1.6	0.7	18.1

exhibited electrode structure collapse and a sharp decrease of capacity, as was also observed in this article.

In addition to SEM/EDS cross-sectional analysis, further postmortem characterizations were carried out by XPS and XRD for completeness. Postmortem XPS analysis of the top of Si-Tit/Gr anode after cycling is shown in Fig. S3. It revealed the presence of C, O, Li and F. There, the presence of Si and Ti is no longer detected. Since it is not possible to separate quantitatively Si nanopowder from the anode composite, this result is not very surprising. The upper anode part is simply mainly composed of SEI species containing carbon, oxygen, lithium and fluorine compounds, which represent traces of the surface
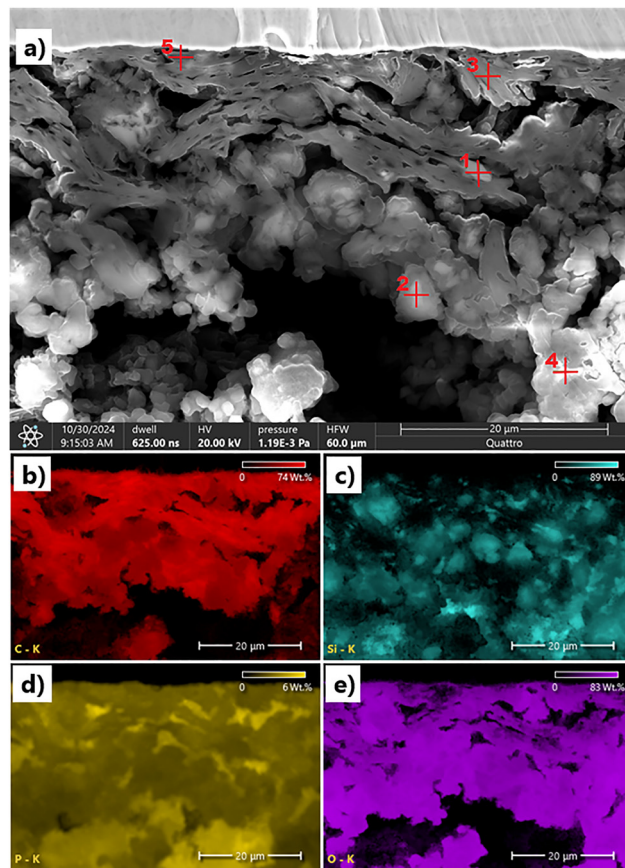
layer formed during cycling. Fig. S4 shows XRD patterns of Si-Tit/Gr anode after cycling and it reveals the presence of carbon (PDF: 00-026-1079), lithium hydroxide hydrate (H_3LiO_2, PDF: 01-076-1074) and copper (PDF: 00-004-0836). Similar as for XPS, even XRD is not able to detect Si nanopowders. The lack of diffraction peaks ascribed to Si confirms the change of structure from crystalline to amorphous after cycling.

Conclusions

In this study, we demonstrated the use of highly doped p-type wafer as a primary source of anode material for Li-ion batteries.

Metal assisted catalytic etching (MACE) introduced 15–20 nm pores into the Si particles, which were subsequently coated with a thin layer of titanicone using molecular layer deposition (MLD). The resulting particles served as the basis of a Si/graphite composite, which was used as the anode in a Li-ion battery. The electrodes modified with a titanicone layer exhibited higher activity, higher capacity at different C-rates, and greater stability under long-term cycling than unmodified Si/graphite electrodes. By post-mortem analysis, we demonstrated that electrodes using titanicone-modified Si particles exhibited greater graphite structural stability and that Si particles were relatively well interconnected, which enabled higher conductivity and integrity of the electrode. In the case of electrodes with unmodified Si particles, the Si and graphite particles were separated as the result of cycling. This led to structural instability of the electrode and a reduced contact of individual particles, resulting in a faster capacity drop during cycling. The results unequivocally demonstrated that the titanicone coating improved anode performance beyond what was achieved by nanostructuring and the addition of silicon alone. The use of highly-doped Si as a source of material for LIB production is therefore possible; moreover, it is possible to further optimize the performance of Si anodes with the combination of MACE and MLD.

Author contributions

Tomas Kazda (data curation, formal analysis, methodology, writing – original draft), Raul Zazpe (conceptualization, data curation, writing – original draft), Antonín Šimek (Investigation), Jhonatan Rodriguez-Pereira (data curation), Ondřej Klvač (Investigation), Juliana T. Hetzel (data curation, methodology), Ludek Hromadko (data curation), David Pavlinak (data curation), Sitaramanjaneya Mouli Thalluri (data curation), Mato Knez (conceptualization, writing – review & editing, supervision, funding), Kurt W. Kolasinski (conceptualization, writing – review & editing, supervision) and Jan M. Macak (conceptualization, writing – original draft, funding, supervision).

Conflicts of interest

There are no conflicts to declare.

Data availability

The data are available from the corresponding author upon reasonable request.

Acknowledgements

References

1 F. Degen, M. Winter, D. Bendig and J. Tübke, *Nat. Energy*, 2023, **8**, 1284–1295.
2 J. Xu, X. Cai, S. Cai, Y. Shao, C. Hu, S. Lu and S. Ding, *Energy Environ. Mater.*, 2023, **6**, 5.
3 H. F. Andersen, C. E. L. Foss, J. Voje, R. Tronstad, T. Mokkelbost, P. E. Vullum, A. Ulvestad, M. Kirkengen and J. P. Mæhlen, *Sci. Rep.*, 2019, **9**, 9.
4 A. Kohandehghan, P. Kalisvaart, K. Cui, M. Kupsta, E. Memarzadeh and D. Mitlin, *J. Mater. Chem. A*, 2013, **1**, 11.
5 L. Sun, Y. Liu, R. Shao, J. Wu, R. Jiang and Z. Jin, *Energy Storage Mater.*, 2022, **46**, 482–502.
6 S. You, H. T. Tan, L. Wei, W. Tan and C. Chao Li, *Chem. – Eur. J.*, 2021, **27**, 12237–12256.
7 A. S. Aricò, P. Bruce, B. Scrosati, J.-M. Tarascon and W. van Schalkwijk, *Nat. Mater.*, 2025, **4**, 366–377.
8 H.-C. Shin, J. A. Corno, J. L. Gole and M. Liu, *J. Power Sources*, 2025, **139**, 314–320.
9 D.-K. Kang, J. A. Corno, J. L. Gole and H.-C. Shin, *J. Electrochem. Soc.*, 2008, **155**, 4.
10 H. Kim, B. Han, J. Choo and J. Cho, *Angew. Chem., Int. Ed.*, 2008, **47**, 10151–10154.
11 M. Leisner, A. Cojocaru, E. Ossei-Wusu, J. Carstensen and H. Föll, *Nanoscale Res. Lett.*, 2010, **5**, 1502–1506.
12 H. Han, Z. Huang and W. Lee, *Nano Today*, 2014, **9**, 271–304.
13 M. J. Armstrong, C. O'Dwyer, W. J. Macklin and J. D. Holmes, *Nano Res.*, 2014, **7**, 1–62.
14 C. K. Chan, H. Peng, G. Liu, K. McIlwrath, X. F. Zhang, R. A. Huggins and Y. Cui, *Nat. Nanotechnol.*, 2008, **3**, 31–35.
15 U. Kasavajjula, C. Wang and A. J. Appleby, *J. Power Sources*, 2007, **163**, 1003–1039.
16 X. H. Liu, L. Zhong, S. Huang, S. X. Mao, T. Zhu and J. Y. Huang, *ACS Nano*, 2012, **6**, 1522–1531.
17 W. McSweeney, H. Geaney and C. O'Dwyer, *Nano Res.*, 2015, **8**, 1395–1442.
18 K. W. Kolasinski, *Micromachines*, 2021, **12**, 18.
19 V. Chirvony, A. Chyrvonaya, J. Ovejero, E. Matveeva, B. Goller, D. Kovalev, A. Huygens and P. de Witte, *Adv. Mater.*, 2007, **19**, 2967–2972.
20 S. Limaye, S. Subramanian, B. Goller, J. Diener and D. Kovalev, *Phys. Status Solidi A*, 2007, **204**, 1297–1301.
21 A. Loni, D. Barwick, L. Batchelor, J. Tunbridge, Y. Han, Z. Y. Li and L. T. Canham, *Electrochem. Solid-State Lett.*, 2011, **14**, K25–K27.
22 E. G. Chadwick, N. V. V. Mogili, C. O'Dwyer, J. D. Moore, J. S. Fletcher, F. Laffir, G. Armstrong and D. A. Tanner, *RSC Adv.*, 2013, **3**, 19393–19402.

23 K. W. Kolasinski, B. A. Unger, A. T. Ernst and M. Aindow, *Front. Chem.*, 2019, **6**, 651.

24 T. Nakamura, N. Hosoya, B. P. Tiwari and S. Adachi, *J. Appl. Phys.*, 2010, **108**, 104315.

25 T. Nakamura, B. P. Tiwari and S. Adachi, Chemical Etching, *Jpn. J. Appl. Phys.*, 2011, **50**, 081301.

26 Y. Liu, B. Chen, F. Cao, H. L. W. Chan, X. Zhao and J. Yuan, *J. Mater. Chem.*, 2011, **21**, 17083.

27 B. M. Bang, H. Kim, H.-K. Song, J. Cho and S. Park, *Energy Environ. Sci.*, 2011, **4**, 5013–5019.

28 Z. Huang, R. Wang, D. Jia, L. Maoying, M. G. Humphrey and C. Zhang, *ACS Appl. Mater. Interfaces*, 2012, **4**, 1553–1559.

29 R. Ouertani, A. Hamdi, C. Amri, M. Khalifa and H. Ezzaouia, *Nanoscale Res. Lett.*, 2014, **9**, 1–10.

30 M. A. Green, WO 2009/010758 A2, 2009.

31 M. Loveridge, M. Lain, F. Liu, F. Coowar, B. Macklin and M. Green, High Performance Silicon Anode Materials For Next Generation Lithium Ion Batteries, in: The 15Th International Meeting On Lithium Batteries – Imlb 2010, IMLB, Montreal, Quebec, Canada, 2010: p. 1.

32 Y. Zhao, X. Liu, H. Li, T. Zhai and H. Zhou, *Chem. Commun.*, 2012, **48**, 5079–5081.

33 G. E. Blomgren, *J. Electrochem. Soc.*, 2017, **164**, A5019–A5025.

34 J.-I. Lee and S. Park, *Nano Energy*, 2013, **2**, 146–152.

35 F. Mattelaer, P. M. Vereecken, J. Dendooven and C. Detavernier, *Adv. Mater. Interfaces*, 2017, **4**, 1601237.

36 H. Sopha, G. D. Salian, R. Zazpe, J. Prikryl, L. Hromadko, T. Djenizian and J. M. Macak, *ACS Omega*, 2017, **2**, 2749–2756.

37 I. Lahiri, S.-M. Oh, J. Y. Hwang, C. Kang, M. Choi, H. Jeon, R. Banerjee, Y.-K. Sun and W. Choi, *J. Mater. Chem.*, 2011, **21**, 13621–13626.

38 Y. S. Jung, A. S. Cavanagh, L. A. Riley, S.-H. Kang, A. C. Dillon, M. D. Groner, S. M. George and S.-H. Lee, *Adv. Mater.*, 2010, **22**, 2172–2176.

39 J. Li, Y. Huang, W. Huang, J. Tao, F. Lv, R. Ye, Y. Lin, Y. Yang Li, Z. Huang and J. Lu, *Small*, 2021, **17**, 2006373.

40 P. P. Sahoo, A. Güneren, B. Hudec, M. Mikolášek, A. Nada, M. Precnerová, M. Mičušík, Z. Lenčéš, P. Nádaždy and K. Fröhlich, *ACS Appl. Nano Mater.*, 2024, **7**, 18486–18498.

41 J. Fang, J. Li, W. Zhang, L. Qin, K. Wu, L. Hui, T. Gong, D. Li, Y. Hu, A. Li and H. Feng, *Chem. Eng. J.*, 2024, **484**, 10.

42 P. Sundberg and M. Karppinen, *Beilstein J. Nanotechnol.*, 2014, **5**, 1104–1136.

43 J. Multia and M. Karppinen, *Adv. Mater. Interfaces*, 2022, **9**, 39.

44 A. I. Abdulagatov, R. A. Hall, J. L. Sutherland, B. H. Lee, A. S. Cavanagh and S. M. George, *Chem. Mater.*, 2012, **24**, 2854–2863.

45 K. Van de Kerckhove, F. Mattelaer, D. Deduytsche, P. M. Vereecken, J. Dendooven and C. Detavernier, *Dalton Trans.*, 2016, **45**, 1176–1184.

46 C. Zhu, K. Han, D. Geng, H. Ye and X. Meng, *Electrochim. Acta*, 2017, **251**, 710–728.

47 T. Mu, Y. Zhao, C. Zhao, N. G. Holmes, S. Lou, J. Li, W. Li, M. He, Y. Sun, C. Du, R. Li, J. Wang, G. Yin and X. Sun, *Adv. Funct. Mater.*, 2021, **31**, 9.

48 L. Luo, H. Yang, P. Yan, J. J. Travis, Y. Lee, N. Liu, D. Molina Piper, S.-H. Lee, P. Zhao, S. M. George, J.-G. Zhang, Y. Cui, S. Zhang, C. Ban and C.-M. Wang, *ACS Nano*, 2015, **9**, 5559–5566.

49 Z. C. Huertas, D. Settipani, C. Flox, J. R. Morante, T. Kallio and J. J. Biendicho, *Sci. Rep.*, 2022, **12**, 137.

50 K. Tamarov, R. Kiviluoto, J. D. Swanson, B. A. Unger, A. T. Ernst, M. Aindow, J. Riikonen, V.-P. Lehto and K. W. Kolasinski, *ACS Appl. Mater. Interfaces*, 2020, **12**, 48969–48981.

51 K. Tamarov, J. D. Swanson, B. A. Unger, K. W. Kolasinski, A. T. Ernst, M. Aindow, V.-P. Lehto and J. Riikonen, *ACS Appl. Mater. Interfaces*, 2020, **12**, 4787–4796.

52 P. G. Rouxhet and M. J. Genet, *Surf. Interface Anal.*, 2011, **43**, 1453–1470.

53 J. F. Moulder, W. F. Stickle, P. E. Sobol and K. D. Bomben, *Handbook of X Ray Photoelectron Spectroscopy: A Reference Book of Standard Spectra for Identification and Interpretation of Xps Data – Hardcover, Physical Electronics*, 2nd edn, 1995.

54 H. Sopha, I. Mirza, H. Turčičova, D. Pavlinak, J. Michalicka, M. Krbal, J. Rodriguez-Pereira, L. Hromadko, O. Novák, J. Mužík, M. Smrž, E. Kolibalova, N. Goodfriend, N. M. Bulgakova, T. Mocek and J. M. Macak, *RSC Adv.*, 2020, **10**, 22137–22145.

55 M. Sepúlveda, J. Musiał, I. Saldan, P. K. Chennam, J. Rodriguez-Pereira, H. Sopha, B. J. Stanisz and J. M. Macak, *Front. Environ. Chem.*, 2024, **5**, 1373320.

56 P. G. Rouxhet and M. J. Genet, *Surf. Interface Anal.*, 2011, **43**, 1453–1470.

57 H. Sopha, J. Bacova, K. Baishya, M. Sepúlveda, J. Rodriguez-Pereira, J. Capek, L. Hromadko, R. Zazpe, S. M. Thalluri, J. Mistrik, P. Knotek, T. Rousar and J. M. Macak, *Surf. Coat. Technol.*, 2023, **462**, 129504.

58 B. Jerliu, E. Hüger, L. Dörrer, B. K. Seidlhofer, R. Steitz, M. Horisberger and H. Schmidt, *Phys. Chem. Chem. Phys.*, 2018, **20**, 23480–23491.

59 C. Heubner, T. Liebmann, O. Lohrberg, S. Cangaz, S. Maletti and A. Michaelis, *Batteries Supercaps*, 2022, **5**, 11.

60 M. J. Loveridge, M. J. Lain, Q. Huang, C. Wan, A. J. Roberts, G. S. Pappas and R. Bhagat, *Phys. Chem. Chem. Phys.*, 2016, **18**, 30677–30685.

61 J. Fang, J. Li, W. Zhang, L. Qin, K. Wu, L. Hui, T. Gong, D. Li, Y. Hu, A. Li and H. Feng, *Chem. Eng. J.*, 2024, **484**, 149387.

62 M. Muraleedharan Pillai, X. Zhao, N. Kalidas, K. Tamarov and V.-P. Lehto, *Microporous Mesoporous Mater.*, 2024, **367**, 10.

63 S.-B. Son, L. Cao, T. Yoon, A. Cresce, S. E. Hafner, J. Liu, M. Groner, K. Xu and C. Ban, *Adv. Sci.*, 2018, **6**, 8.

64 M. Phadatare, R. Patil, N. Blomquist, S. Forsberg, J. Örtegren, M. Hummelgård, J. Meshram, G. Hernández, D. Brandell, K. Leifer, S. K. M. Sathyanath and H. Olin, *Sci. Rep.*, 2019, **9**, 14621.

65 F. Zhang, L. Wan, J. Chen, X. Li and X. Yan, *Electrochim. Acta*, 2018, **280**, 86–93.

66 M.-S. Wang, G.-L. Wang, S. Wang, J. Zhang, J. Wang, W. Zhong, F. Tang, Z.-L. Yang, J. Zheng and X. Li, *Chem. Eng. J.*, 2019, **356**, 895–903.